Electronic Supplementary Information

# Fabrication of ultrathin two-dimensional MOF nanosheets with cage-like cavities showing excellent adsorption for lead(II)

Hongwei Sun,[a] Ke-Zhong Wang,[a] Meng-Ru Yao,[a] Cai-Xia Yu,*[,a] Yue-Hai Song,[a] Jing Ding,[a] Yan-Li Zhou[a], Dong Liu,*[,b] and Lei-Lei Liu*[,a]

[a] School of Environmental and Material Engineering, Yantai University, Yantai 264005, P. R. China

[b] Jiangsu Key Laboratory for Chemistry of Low-Dimensional Materials, School of Chemistry and Chemical Engineering, Huaiyin Normal University, Huaian 223300, P. R. China

* To whom correspondence should be addressed. E-mail addresses: liuleileimail@163.com (L.-L. Liu).

**Table of Contents**

**Section 1. Materials and physical measurements**

**General Procedure.** 25, 26, 27, 28-tetrahydroxycalix[4]arene, ethyl bromoacetate and $K_2CO_3$ were purchased from Meryer Co., Ltd. MeCN, EtOH, MeOH, isopropanol, KOH, $CuCl_2·2H_2O$ and $Pb(NO_3)_2$ were purchased from Sinopharm Chemical Co., Ltd. These chemicals and reagents were obtained from commercial sources and used as received without treatment. Powder X-ray diffraction (PXRD) was performed using a PANalytical X'Pert PRO MPD system (PW3040/60). Thermal analysis was performed with a Netzsch STA-449F3 thermogravimetric analyzer at a heating rate of 10 °C $min^{-1}$ and a flow rate of 20 $cm^3$ $min^{-1}$ ($N_2$). Fourier transform infrared (FT-IR) spectra were recorded on an IR Prestige-21. The FT-IR samples were prepared by blending the compound with KBr and compressing the mixture to obtain transparent sheets. Scanning electron microscopy (SEM) images were taken by a JSM-7610F instrument. X-ray photoelectron spectroscopy (XPS) was performed on a Thermo Escalab 250 spectrometer with monochromated $Al_{K\alpha}$ excitation. The zeta potential was determined using dynamic light scattering (DLS) on Malvern Instruments Nanosizer-ZS.

**Preparation of 25, 26, 27, 28-tetrakis[(carboxyl)methoxy]calix[4]arene ($H_4L$).** $H_4L$ was prepared according to the literature method.[1] 25, 26, 27, 28-tetrahydroxycalix[4]arene (0.98 g, 2.30 mmol), ethyl bromacetate (3.1 mL, 27.96 mmol) and $K_2CO_3$ (3.0 g, 21.7 mmol) were added into acetone (150 mL). The mixture was refluxed for 5 days. After allowing the reaction mixture to cool to room temperature, the solvent was removed under reduced pressure. The residue was then triturated three times with EtOH (25 mL × 3) and filtered off the white solid. The desired white solid was kept in high vacuum overnight. The obtained white solid (0.77 g, 1.0 mmol) and KOH (0.84 g, 15 mmol) in EtOH (50 mL) was heated at reflux for 15 hours. The solution was then allowed to cool to room temperature and evaporated to dryness by rotary evaporation. The residue was added 2 M HCl (30 mL) in an ice-water bath. Precipitate was collected by filtration and washed with water and air-dried, forming a white powder. Yield: 0.57 g (38%, based on 25, 26, 27, 28-tetrahydroxycalix[4]arene).

**Preparation of $\{[Cu_{1.5}(HL)(H_2O)_3]·H_2O\}_n$ (Cu-MOF).** $CuCl_2·2H_2O$ (5.5 mg, 0.032 mmol), $H_4L$ (5.3 mg, 0.008 mmol), and 9 mL $H_2O$/MeCN (8:1 V/V) were placed in a 20 mL glass bottle. The mixture was sonicated for 30 seconds. Then the bottle was sealed and kept in an oven at a temperature of 373 K for 48 hours. After slow cooling down to room temperature, green block crystals of **Cu-MOF** were obtained, which were washed with distilled water and dried at room temperature. Yield: 3.0 mg (46%, based on $H_4L$). The above 3.0 mg scale was for single crystal diffraction. More bulk **Cu-MOF** can be synthesized at a time as follows: $CuCl_2·2H_2O$ (54.6 mg, 0.32 mmol), $H_4L$ (52.5 mg, 0.08 mmol), and 90 mL $H_2O$/MeCN (8:1 V/V) were placed in a 150 mL glass bottle; the subsequent operations were similar with the above method. Yield: 32.6 mg (50%, based on $H_4L$). Anal. Calcd for

$C_{36}H_{37}Cu_{1.5}O_{16}$: C, 52.67; H, 4.54. Found: C, 52.35; H, 4.66.

**Preparation of 2D Cu-MOF nanosheets.** Firstly, the bulk **Cu-MOF** was ground for about 1 hour. Secondly, the ground MOF samples were activated by heating at 373 K (12 hours) under a vacuum to remove the encapsulated solvent guests. Thirdly, 20 mg of the as-prepared MOF was dispersed in 40 mL of MeOH/isopropanol (4:1, V/V) and sonicated in an ice-water bath for 6 hours. After sedimentation for 1 hour, the upper colloidal suspension was centrifugated at 10000 rpm at 278 K to get the exfoliated 2D MOF nanosheets, which were then collected and dried in the air.

**X-ray crystal structure determination.** Single X-ray diffraction intensities of crystal were collected on a CCD diffractometer at 150 K. All diffractometers were equipped with a graphite monochromated Mo-Kα radiation (λ = 0.71073). The structure was solved by the direct method and expanded with the Fourier technique. All calculations were performed with SHELXL-97 package. All H atoms in **Cu-MOF** were placed in geometrically idealized positions and constrained to ride on their parent atoms. The crystal data for **Cu-MOF** was summarized as follows: $C_{72}H_{74}Cu_3O_{32}$, Mr = 1641.96, monoclinic, space group *C*2/*c*, $a$ = 38.299(8) Å, $b$ = 11.554(2) Å, $c$ = 16.669(3) Å, $\alpha$ = 90°, $\beta$ = 108.55(3)°, $\gamma$ = 90°, $V$ = 6993(3) Å$^3$, $Z$ = 4, $D_c$ = 1.560 g cm$^{-3}$, $F(000)$ = 3396.0 and $\mu$ = 0.998 mm$^{-1}$, 35929 reflections collected, 6145 unique ($R_{int}$ = 0.0396). $R_1$ = 0.0369, $wR_2$ = 0.1090 and S = 1.034. Crystallographic data have been submitted to the Cambridge Structural Database with deposition number CCDC 2206848.

**TEM and AFM characterizations.** Prior to the characterizations of transmission electron microscopy (TEM) and atomic force microscopy (AFM), 3 mg of the as-prepared MOF was dispersed in 10 mL of MeOH/isopropanol (4:1, V/V) and sonicated in an ice-water bath for 6 hours. After sedimentation for 12 hours, the upper colloidal suspension of 2D nanosheets was dropped onto the holey carbon-coated carbon support copper grids and mica, respectively, and then naturally dried in the air. TEM images were operated at an acceleration voltage of 200 kV (JEOL JEM 2100). AFM images were obtained on a dimension edge microscope (Bruker Edge) equipped with a tapping mode.

**Section 2. Adsorption experiments**

**$Pb^{2+}$ adsorption studies.** The $Pb^{2+}$ sorption experiments were performed in 50 mL $Pb^{2+}$ standard solution at 298 K under continuous stirring, by employing 5 mg of MOF nanosheets as adsorbents. Analytical samples were taken at given time intervals and measured with atomic absorption spectrometer (AAS) and/or inductively coupled plasma-mass spectrometry (ICP-MS). To analyze the effect of pH, the adsorbent (5 mg) was added to 50 mL of 10 ppm $Pb^{2+}$ solution, the sorption tests were conducted under different pH conditions (3.0-7.0) adjusted by $HNO_3$ or NaOH solutions. The adsorption isotherm experiments were investigated by adding 5 mg MOF nanosheets into 50 mL $Pb^{2+}$ solutions with different concentrations to reach adsorption equilibrium.

The recyclability was further evaluated by the regeneration test. In each cycle, the $Pb^{2+}$-loaded nanosheets were separated and immersed in a flask containing 80 mL of $HNO_3$ solution (0.1 mmol $L^{-1}$) for desorption. After immersion in $HNO_3$ solution for 36 hours, the samples were washed with deionized water three times. Then the products were dried under vacuum for the following test. The method determining the desorbed $Pb^{2+}$ was the same as the adsorption studies.

The adsorption capacity $q_t$ (mg $g^{-1}$) and the removal efficiency were calculated as followings:

$$q_t = \frac{(C_0 - C_t)V}{m} \quad \textbf{(S1)}$$

$$\text{Removal efficiency (\%)} = \frac{C_0 - C_e}{C_0} \times 100\% \quad \textbf{(S2)}$$

where $C_0$ (mg $L^{-1}$) and $C_e$ (mg $L^{-1}$) represent the solution concentrations of $Pb^{2+}$ at the initial and equilibrium stages, respectively. $V$ (L) represents solution volume; $m$ (g) is the amount of adsorbent after drying treatment.

The Langmuir and Freundlich isotherm model were employed to simulate the adsorption isotherm data and can be described as:

$$\frac{C_e}{q_e} = \frac{C_e}{q_m} + \frac{1}{q_m K_L} \quad \textbf{(S3)}$$

$$\ln q_e = \ln K_F + \frac{1}{n} \ln C_e \quad \textbf{(S4)}$$

where $q_e$ (mg $g^{-1}$) is the adsorption amounts at equilibrium and $C_e$ (mg $L^{-1}$) is the equilibrium concentration of $Pb^{2+}$. $q_m$ (mg $g^{-1}$) is the maximum amount or the saturated adsorption amount. $K_L$ (L $mg^{-1}$) is the Langmuir constant, quantitatively reflecting the affinity of binding sites to the energy of adsorption. $K_F$ ((mg $g^{-1}$)/(L $mg^{-1})^{1/n}$) is the Freundlich constant which indicates the adsorption capacity and n is an empirical parameter related to the intensity of adsorption. The Langmuir model assumes that the solid surface active sites can be occupied only by one layer of

adsorbates and there is no interaction between the adsorbate molecules. On the contrary, the Freundlich model is based on heterogeneous adsorption.

To assess the sorbent's affinity for $Pb^{2+}$, the distribution coefficient $K_d$ (mL $g^{-1}$) was calculated according to the following equation:

$$K_d = \frac{(C_0 - C_e)}{C_e} \times \frac{V}{m} \quad \textbf{(S5)}$$

where $C_0$ (mg $L^{-1}$) and $C_e$ (mg $L^{-1}$) represent the solution concentrations of $Pb^{2+}$ at the initial and equilibrium stages, respectively. $V$ (mL) represents solution volume, $m$ (g) is the amount of adsorbent after drying treatment.

**Section 3. Calculation method**

**Adsorption model calculation**. The density functional theory (DFT) calculation was performed to better elucidate the electronic and structural properties and atomic interactions between $Pb^{2+}$ and **Cu-MOF**. Cage-like second building units (SBU) is suitable as model for **Cu-MOF** due to the time-consuming nature of DFT calculations. The theoretical calculations were conducted by ignoring the solvating effect and $Pb^{2+}$ was only considered as an interacting adsorbate with carboxylate and ether functional adsorbents.

The Gaussian 16 suite of programs[2] was used to optimize the configurations. Structural optimization was performed using the B3LYP functional with the def2-SVP basis set. The Gibbs free energy (ΔG) of $Pb^{2+}$ on SBU can be obtained by BSSE correction. The formula is as follows:

$$\Delta G_{ads} = G_{(SBU+Pb^{2+})} - G_{(SBU)} - G_{(Pb^{2+})}$$

where $G_{(SBU+Pb^{2+})}$, $G_{(SBU)}$, and $G_{(Pb^{2+})}$ represent the total energies of the SBU + $Pb^{2+}$ system, SBU, and $Pb^{2+}$, respectively.

**Selectivity calculation**. The first-principles calculations were performed using the Vienna Ab initio Simulation Package (VASP)[3-4] for the selectivity adsorption calculation. The generalized gradient approximation (GGA) with the functional described by Perdew-Burke-Ernzerhof (PBE) functional was used for structure optimization.[5] The convergence criteria for SCF and force during geometry optimization was set as $10^{-5}$ eV and 0.02 eV $Å^{-1}$. Then frequency calculation was followed to obtain the Gibbs free energetics, with only adsorbates allowed for the numerical difference.

The adsorption energy ($E_{ads}$) was defined by the following equation:

$$\Delta E_{ads} = E_{(SBU+M^{n+})} - E_{(SBU)} - E_{(M^{n+})}$$

where $E_{(SBU+M^{n+})}$, $E_{(SBU)}$, and $E_{(M^{n+})}$ represents the total energy of heavy metals on SBU, SBU, and metal ions, respectively. $M^{n+}$ = $Pb^{2+}$, $Na^{+}$, $K^{+}$, $Ca^{2+}$, $Mg^{2+}$, $Sr^{2+}$, $Co^{2+}$, $Ni^{2+}$, $Cd^{2+}$, and $Ba^{2+}$.

**Section 4. Supporting Tables**

**Table S1.** Adsorption constants for Langmuir and Freundlich isotherm models.

| | Langmuir | | | Freundlich | | |
|---|---|---|---|---|---|---|
| T/K | $q_{max}$ | $K_L$ | $R^2$ | $K_F$ | n | $R^2$ |
| 298 | 746.26 | 0.489 | 0.999 | 216.16 | 0.275 | 0.673 |

**Table S2.** Comparison of $Pb^{2+}$ maximum uptake capacity, dominant adsorption mechanism and selective adsorption mechanism for **Cu-MOF** nanosheets and bulk **Cu-MOF** with various adsorbents.

| Adsorbents | Maximum uptake capacity (mg $g^{-1}$) | Dominant mechanism | Selective adsorption mechanism | Ref. |
|---|---|---|---|---|
| TMU-32 | 909 | Coordination interaction | n.a. | 6 |
| Cd-MOF | 845.55 | Coordination, electrostatic interactions | Hydration energy | 7 |
| HKUST-1 | 819.28 | Coordination interaction, ion exchange | HSAB/hydration energy/ionic radius | 8 |
| **Cu-MOF nanosheets** | **738.65** | Coordination, electrostatic interactions | HSAB/hydration energy/ionic radius | **this work** |
| Cu-BTC-Th | 732.86 | Coordination interaction, ion exchange | n.a. | 9 |
| β-CDPP | 576.92 | Coordination, electrostatic interactions | n.a. | 10 |
| Fe doped HKUST-1 | 565 | Ion exchange | Hydration energy/ionic radius | 11 |
| Pr-MOF | 560.26 | Coordination, electrostatic interactions | HSAB/hydration energy/ionic radius | 12 |
| JUC-505-COOH | 559 | Coordination, H-bonding interactions | Ionic radius | 13 |
| p-UCR-20 | 527 | Coordination interaction | HSAB | 14 |
| **Bulk Cu-MOF** | **509.56** | Coordination, electrostatic interactions | HSAB/hydration energy/ionic radius | **this work** |
| CSt-ZnO | 476 | Coordination interaction | n.a. | 15 |
| Zn-MOF | 463.52 | Coordination, electrostatic interactions | Hydration energy/ionic radius | 16 |
| Co-Al-LDH@$Fe_2O_3$/DPCNF | 426.76 | Surface complexation, precipitation, isomorphic substitution | n.a. | 17 |
| UiO-66-ATA(Zr) | 386.98 | Coordination, electrostatic interactions, ion exchange | HSAB/Hofmeister | 18 |
| TMU-74 | 385.71 | Coordination interaction | n.a. | 19 |
| PAMAM@UiO-66-$NH_2$ | 334.32 | Coordination interaction | HSAB | 20 |

| | | | | |
|---|---|---|---|---|
| MIL-125-HQ | 262.1 | Coordination interaction | n.a. | 21 |
| UiO-66-$(COOH)_2$ | 254.5 | Coordination interaction | n.a. | 22 |
| $MnO_2$/PDA/$Fe_3O_4$ fibers | 205.07 | Coordination interaction | n.a. | 23 |
| Ti/Zr-DBMD | 175 | Coordination, electrostatic interactions | Electronegativity/ionic radius/ /hydration radius/hydration energy | 24 |
| Mg doped Fh-HA | 120.43 | Coordination interaction | n.a. | 25 |
| PVA/GO/ZIF-67 | 106.8 | Coordination interaction | n.a. | 26 |
| DUT-67 | 98.5 | Coordination interaction | n.a. | 27 |
| CMP-3a | 93.2 | Coordination, electrostatic, H-bonding interactions | Electronegativity/ionic radius | 28 |
| CMP-2a | 62.7 | Coordination, electrostatic, H-bonding interactions | Electronegativity/ionic radius | 28 |

n.a. represents the information not available.

Based on the above, $Pb^{2+}$ adsorption mechanism mainly includes coordination interaction, electrostatic interaction, ion exchange and H-bonding interaction. These adsorbents generally involved one or more of these adsorption mechanisms. For the selective adsorption performance, some of them did not mention. The mentioned selective adsorption performance were cited in the following part according to the order in the table, together with the specific selective adsorption mechanism.

**Reference 7**: For Cd-MOF, the selective adsorption of metal ions is conducted between different kinds of ions ($Hg^{2+}$, $Cu^{2+}$, $Pb^{2+}$, *etc*.) with a concentration of 100 mg/L. Studies shows that the Cd-MOF has a specific and selective adsorption for $Pb^{2+}$. We also verify the removal efficiency of the Cd-MOF for $Pb^{2+}$ in mixed ions solution, since numerous ions exist in domestic and industrial wastewater ($M^{n+}$ = 200 mg/L, $Cl^-$ > 200 mg/L, $NO_3^-$ >200 mg/L). We refer to the possible components of actual sewage and configure a mixed solution containing a certain concentration of interfering ions such as $Hg^{2+}$ ions and $Cd^{2+}$ ions. The Cd-MOF has excellent anti-interference ability, and the removal rate of $Pb^{2+}$ can still reach 90% under the coexistence of various ions. The selectivity of the Cd-MOF to $Pb^{2+}$ can be attributed to the following reasons: (1) The uncoordinated N and the uncoordinated O on $SO_4^{2-}$ provide the driving force for the interaction between $Pb^{2+}$; (2) Metal ions must dissociate most of the water of hydration before being adsorbed, so $Pb^{2+}$ (1425 kJ/mol for $Pb^{2+}$, 1760 kJ/mol for $Hg^{2+}$) with lower hydration energy is easier to be adsorbed.

**Reference 8**: For HKUST-1, the selective $Pb^{2+}$ adsorption performance were evaluated by comparison of the removal efficiency of HKUST-1 towards some divalent metallic ions, including the $Cd^{2+}$, $Pb^{2+}$, $Ni^{2+}$, $Mn^{2+}$, $Ca^{2+}$ and $Zn^{2+}$. Specifically, 10 mg of HKUST-1 was respectively dispersed in a coexisting ions solution containing $Ni^{2+}$,

$Cd^{2+}$, $Pb^{2+}$, $Zn^{2+}$, $Mn^{2+}$ and $Ca^{2+}$. The concentration of each metal ion mixture was fixed at 100 mg/L. The removal efficiency of $Pb^{2+}$ was significantly higher than that of other metal ions, suggesting that the HKUST-1 showed great selectivity towards $Pb^{2+}$. There are several reasons related to the strong excellent selectivity of HKUST-1 towards $Pb^{2+}$. Firstly, the high removal efficiency of $Pb^{2+}$ can be attributed to its relatively lower hydration energy (-ΔH) (1481 kJ/mol), as compared to $Ca^{2+}$ (1577 kJ/ mol), $Mn^{2+}$ (1845.6 kJ/mol), $Ni^{2+}$ (2106 kJ/mol), $Cd^{2+}$ (1807 kJ/mol) and $Zn^{2+}$ (2057 kJ/mol). Among these divalent cations, the hydration radius of $Pb^{2+}$ was the largest, which could also determine its strongest cation affinity. Besides, $Pb^{2+}$, as the borderline acids, was likely to bind to the oxygen-containing functional groups of the ligands retained on the channel surface freely instead of binding with the metal center, according to the hard-soft acid-base theory (HSAB).

**Reference 11**: The selectivity and specificity studies of undoped and Fe doped HKUST-1 towards $Pb^{2+}$ ions was carried out in a mixed solution containing $Na^{+}$, $Mg^{2+}$, $Ca^{2+}$, and $Pb^{2+}$. Figure shows that there was 95%, 91% and 83% removal of $Pb^{2+}$ ions from HKUST-1, $Fe_{0.05}$HKUST-1 and $Fe_{0.1}$HKUST-1 MOF respectively in presence of 50 mg/L counter ions, while a negligible amount of $Na^{+}$, $Ca^{2+}$ and $Mg^{2+}$ ions removal was observed. The high removal efficiency of $Pb^{2+}$ in presence of counter ions was observed due to its low hydration energy (-ΔH) (1481 kJ/mol) and high hydration radius (2.57 Å), as compared to hydration energy and hydration radius of counter ions ($Mg^{2+}$ (1921 kJ/mol, 1.85 Å), $Ca^{2+}$ (1577 kJ/mol, 2.27 Å) and $Na^{+}$ (409 kJ/mol, 2.21 Å). Large hydration energy and small hydration radius, makes it difficult for the ions to pass through the porous networks of the MOF, hindering the ion exchange from the active sites.

**Reference 12**: For Pr-MOF, the selective experiments were performed in a mixture of metal ions ($Na^{+}$, $K^{+}$, $Sr^{2+}$, $Ni^{2+}$, $Mn^{2+}$, $Co^{2+}$, $Cd^{2+}$, $As^{3+}$ and $As^{5+}$), with an initial concentration of 10 ppm for each one. As shown in Figure, after adding the MOF adsorbents into the mixed solution, the sorption capacity for $Pb^{2+}$ was 46.21 mg $g^{-1}$, while for other ions, the uptake capacities were less than 1.0 mg $g^{-1}$. This result illustrates that Pr-MOF has a high selectivity for $Pb^{2+}$ adsorption. This phenomenon is more in line with the HSAB principle. All factors being equal, a “soft” acid reacts more readily with a “soft” base, while a “hard” acid reacts more readily with a “hard” base, by the formation of stronger bonds. The $O^{-}$ group in the adsorbent, had the property of a borderline base, which could readily interact with borderline acids ($Ni^{2+}$, $Co^{2+}$, and $Pb^{2+}$), but not easy with hard acids ($Mn^{2+}$, $Sr^{2+}$, $Na^{+}$, $K^{+}$, $As^{3+}$ and $As^{5+}$) and soft acid ($Cd^{2+}$). Nevertheless, an obviously lower uptake capacity was obtained for the borderline acids $Co^{2+}$ and $Ni^{2+}$, by comparison with $Pb^{2+}$. This was due to the fact that $Co^{2+}$ and $Ni^{2+}$ hold relatively high binding energy for water molecules ($Co^{2+}$ -1915 kJ/mol; $Ni^{2+}$-1980 kJ/mol), while the binding energy for $Pb^{2+}$ is 1425 kJ/mol. The higher binding energy made it more difficult for $Co^{2+}$ and $Ni^{2+}$ to separate from water molecules

and further interact with the adsorption groups of $O^-$. Moreover, the obvious larger radius of $Pb^{2+}$ (0.119 nm) provides convenience for the interaction with $O^-$ groups, which endows Pr-MOF with high selectivity for $Pb^{2+}$ adsorption.

**Reference 13**: For JUC-505-COOH, the selective adsorption performance toward $Cd^{2+}$ and $Pb^{2+}$ in the presence of five concomitant ions ($NO_3^-$, $SO_4^{2-}$, $Na^+$, $Ca^{2+}$, $Mg^{2+}$) ubiquitously co-existing in natural water, in order to evaluate the anti-interference adsorption ability of JUC-505-COOH in complex natural conditions. As shown in Figure, the removal of $Cd^{2+}$ and $Pb^{2+}$ is hardly affected by the common acid radical ions ($NO_3^-$, $SO_4^{2-}$) and monovalent metal ions ($Na^+$). Both the removal efficiencies for $Cd^{2+}$ and $Pb^{2+}$ can reach to 98.56-99.89%, when the initial concentration is 10 mg/L and the concomitant ions ($NO_3^-$, $SO_4^{2-}$, $Na^+$) concentrations are 10-500 mg/L. For divalent cations, because they have the same positive charge number, comparable ions size and charge density as $Cd^{2+}$, they have more possibility to affect the adsorption of $Cd^{2+}$. It is probably because that it is more easily for $Pb^{2+}$ ions to obtain electrons from the adsorbent due to the relatively bigger electronic cloud size.

**Reference 14**: For p-UCR-20, the selectivity of p-UCR-20 for $Pb^{2+}$ over other heavy metal ions have examined. Experiments were conducted in 10 mL distilled water containing a mixture of $Pb^{2+}$, $Ni^{2+}$, $Cd^{2+}$, $Zn^{2+}$ and $Cu^{2+}$ (each with an initial concentration of 1 ppm) and 10 mg of p-UCR-20. The removal percentages were calculated to be 99.95%, 93.00%, 99.74%, 77% and 82.36% for $Pb^{2+}$, $Ni^{2+}$, $Cd^{2+}$, $Zn^{2+}$ and $Cu^{2+}$, respectively. In addition, the sorption of $Pb^{2+}$ by p-UCR-20 in either batch or continuous flow conditions is not affected by the presence of several cationic species such as $H^+$, $Na^+$, $Ca^{2+}$, $Mg^{2+}$ *etc*. This is attributed to the particularly weak interactions of hard cations with the soft sulfide-based framework of p-UCR-20. In contrast, the latter interacts particularly strongly with the soft $Pb^{2+}$, thus leading to the exceptional selectivity of p-UCR-20 towards this cation.

**Reference 16**: For Zn-MOF, to test the selectivity, adsorbents were added into the mixed solution containing various metal ions ($Na^+$, $Mg^{2+}$, $K^+$, $Ca^{2+}$, $Mn^{2+}$, $Co^{2+}$, $Ni^{2+}$, $Cd^{2+}$, and $Pb^{2+}$) with the same concentration of 10 ppm. As presented in Figure, the removal efficiency for $Pb^{2+}$ significantly exceeds those of other ions. In the mixed solution, 99.05% $Pb^{2+}$ was adsorbed, while the removal efficiencies of other coexisting ions (except $Cd^{2+}$) were less than 5%. For $Cd^{2+}$, the removal efficiency was 10.62%. By comparison with the soft acid of $Cd^{2+}$, which has a comparable charge density and ionic size to $Pb^{2+}$, an ultrahigh selectivity obtained for $Pb^{2+}$ can be attributed to the following reasons: (1) the interactions between $O^-$ groups of MOF adsorbents and $Pb^{2+}$ provided the strong driving force for $Pb^{2+}$ sorption. (2) The metal ions with a lower hydration energy (1425 kJ/mol for $Pb^{2+}$, 1755 kJ/mol for $Cd^{2+}$) tend to be adsorbed, as they have to detach a large part of hydrated water before entering the relatively small channels of adsorbents. (3) The larger ionic radius of metal ions (0.119 nm for $Pb^{2+}$, 0.095 nm for $Cd^{2+}$) would

facilitate the interaction with the functional groups of adsorbents.

**Reference 18**: Usually, many heavy metal ions coexist with $Pb^{2+}$ in wastewater and may affect the sorption properties of UiO-66-ATA(Zr). This section explores the selectivity of adsorbents, and the results are shown in Figure. As observed, the removal rates of all of the coexisting ions were not comparable to that of $Pb^{2+}$, and the adsorption capacity of $Pb^{2+}$ (99.766 mg/g) was higher than that of other metal ions. Based on the HSAB law, hard bases could form stable hard-hard bonds with hard acids, while soft bases with soft acids and borderline acids could form stable hard-hard or soft-soft bonds with both. Thus, $Pb^{2+}$, $Cd^{2+}$, $Ni^{2+}$, $Co^{2+}$, and $Zn^{2+}$ are the metals of borderline acids and might interact more easily with the groups of nitrogen (hard)/sulfur (soft)/oxygen (hard) than $Te^{2+}$, $Mg^{2+}$, and $Fe^{3+}$. In addition, UiO-66-ATA(Zr) contained oxygen, sulfur, and nitrogen groups, which provided the basic support for $Pb^{2+}$ adsorption. According to the Hofmeister effect, meanwhile, some reported works illustrated that the chemisorption ability of some borderline acid metals obeyed the sequence of $Pb^{2+} > Cd^{2+}$, $Pb^{2+} > Ni^{2+}$, $Pb^{2+} > Co^{2+}$, $Pb^{2+} > Zn^{2+}$, which further corroborated the better adsorption capacity and efficiency of Pb(II) onto UiO-66-ATA(Zr). Therefore, $Pb^{2+}$ was like a crane standing among chickens, and the sorption properties of UiO-66-ATA(Zr) for $Pb^{2+}$ were improved.

**Reference 20**: For PAMAM@UiO-66-$NH_2$, the selective adsorption of the adsorbent to $Pb^{2+}$ was verified by an adsorption experiment on polluted water, in which multiple metal ions coexisted. PAMAM@UiO-66-$NH_2$ (10 mg) was immersed in 10 mL of polluted water containing $Pb^{2+}$, $Cu^{2+}$, $Zn^{2+}$, $Cd^{2+}$, $Ni^{2+}$, and $Mg^{2+}$. First, the concentration of various metal ions in the sewage was tested at pH 4 before the experiment, and then the adsorbed supernatant was used to detect the remaining metal ion concentrations. Compared to UiO-66-$NH_2$, PAMAM@UiO-66-$NH_2$ showed strong preferential selectivity for $Pb^{2+}$. Figure shows that PAMAM@UiO-66-$NH_2$ has excellent selectivity for $Pb^{2+}$ and a high removal rate (83.76 mg/g) in the presence of multiple metal ions. In contrast, the native format of UiO-66- $NH_2$ showed poor selectivity for most of the examined metal ions. According to the hard-soft acid-base theory (HSAB), the amino groups on the surface of PAMAM belong to soft bases, which makes it easier to form stable soft-soft bonds with metal ions belonging to soft acids. In the mixed solution, $Pb^{2+}$ was associated with stearic acid, and the interaction with the amino group was weak. In addition, the absolute hardness of the other boundary acids in the solution was greater than that of $Pb^{2+}$. Therefore, PAMAM@UiO-66-$NH_2$ is more likely to interact with $Pb^{2+}$, demonstrating the selectivity of the adsorbent for $Pb^{2+}$.

**Reference 24**: For Ti/Zr-DBMD, the selective adsorption performance was investigated in a mixed solution including $Pb^{2+}$, $Mg^{2+}$, $Ni^{2+}$, $Zn^{2+}$, $Cd^{2+}$ and $Ca^{2+}$. The 40 mL mixture was shaken for 24 h after 40 mg of Ti/Zr-DBMD was added. After adsorption equilibrium, the concentration of each metal ion was determined. The

adsorption capacity were $Pb^{2+}$ (19.2 mg/L), $Mg^{2+}$ (0.3 mg/L), $Ni^{2+}$ (0.2 mg/L), $Zn^{2+}$ (0.4 mg/L), $Cd^{2+}$ (0.9 mg/L) and $Ca^{2+}$ (0.2 mg/L). The selective capture capacity of $Pb^{2+}$ in the coexisting solution was substantially greater than that of other metal cations. The physicochemical properties included electronegativity (**Xm**), ionic radius (**IR**), and atomic weight (**AW**), hydration radius and hydration energy. The larger the atomic weight of the ion, the stronger the adsorption affinity. Among many ions, $Pb^{2+}$ had the largest **AW** (207.19), which made it preferentially adsorbed. The **Xm** of $Pb^{2+}$, $Ca^{2+}$, $Ni^{2+}$, $Zn^{2+}$, $Mg^{2+}$ and $Cd^{2+}$ were 2.33, 1, 1.9, 1.81, 1.31 and 1.69. As the **Xm** of the ions increased, the electronic attraction to the counter ions also increased. The adsorption capacity was affected by the binding force and the different similarities with the binding sites of metal ions. It was difficult to attribute the adsorption capacity to a single factor such as **IR**. Therefore, the covalent index (**Xm2r**) was introduced. The **Xm2r** of $Pb^{2+}$, $Ca^{2+}$, $Ni^{2+}$, $Zn^{2+}$, $Mg^{2+}$ and $Cd^{2+}$ were 6.41, 1, 2.49, 2.42, 1.24 and 2.71. According to reports, the adsorption capacity was positively correlated with **Xm2r**. The largest **Xm2r** value indicated the strongest interaction between Ti/Zr-DBMD and $Pb^{2+}$. In addition, metal ion affinity for Ti/Zr-DBMD was strongly linked to hydration radius and hydration energy. The hydration radius of $Pb^{2+}$, $Ca^{2+}$, $Ni^{2+}$, $Zn^{2+}$, $Mg^{2+}$ and $Cd^{2+}$ were 4.01, 4.12, 4.04, 4.30, 4.28 and 4.26 nm. A greater electrostatic attraction would result from a smaller hydration radius. The hydration energy of $Pb^{2+}$, $Ca^{2+}$, $Ni^{2+}$, $Zn^{2+}$, $Mg^{2+}$ and $Cd^{2+}$ were 1513, 1593, 2068, 2043, 1918 and 1843 kJ/mol. The smallest hydration energy meant that among the many ions, the hydration layer around $Pb^{2+}$ was the weakest.

**Reference 28**: For CMP-3a, the selective $Pb^{2+}$ adsorption against $Cu^{2+}$ and $Ni^{2+}$ of CMP-3a was investigated in heavy metal solutions with various concentrations. The removal of $Pb^{2+}$ reached ca. 84% (versus ca. 40% for $Cu^{2+}$ and ca. 18.6% for $Ni^{2+}$) in 50 mL 10 mg/L solutions at dosage of 10 mg. The high adsorption capacity of $Pb^{2+}$ over $Cu^{2+}$ and $Ni^{2+}$ was related to the higher electronegativity value of the $Pb^{2+}$ (Pauling's scale 2.33) compared to that of $Cu^{2+}$ (1.90) and $Ni^{2+}$ (1.91). Moreover, the large amount of delocalized π electrons on cyano groups was available to donate the vacant 6p orbitals of $Pb^{2+}$ ions and thus facilitated more $Pb^{2+}$ adsorption. $Pb^{2+}$ is known to have flexible coordination numbers and uneven coordination geometry, the exposure of lone pair electrons of hydrated $Pb^{2+}$ ions to the host framework of CMP-3a can be significant, and thus coordinative bonds account largely for the fast and high adsorption of $Pb^{2+}$ in both np and lp of the CMP-3a. Because of the multiple and viable host-guest interactions, including hydrogen bonds (HBs) and electrostatic attractions (EAs), and coordination bonds, the highly efficient and selective $Pb^{2+}$ adsorption is extremely superior.

For the above adsorbents, they presented comparable adsorption selectivity. The selective adsorption mechanism mainly includes hard-soft acid-base theory (HSAB), hydration energy and ionic radius. On the one hand, the borderline acids of $Pb^{2+}$ was likely to bind to the oxygen-containing functional groups based on the HSAB theory;

on the other hand, metal ions usually dissociate most of the hydration water before being adsorbed, so the obviously lower hydration energy for $Pb^{2+}$ (1425 kJ $mol^{-1}$), by comparison with the borderline acids of $Co^{2+}$, $Ni^{2+}$ (1915 kJ $mol^{-1}$ for $Co^{2+}$, 1980 kJ $mol^{-1}$ for $Ni^{2+}$) and $Cd^{2+}$ (1755 kJ $mol^{-1}$) made it easier to be adsorbed; moreover, the obviously larger ionic radius (0.119 nm for $Pb^{2+}$, 0.075 nm for $Co^{2+}$, 0.069 nm for $Ni^{2+}$, 0.095 nm for $Cd^{2+}$) facilitated the interaction of $Pb^{2+}$ with the functional groups on adsorbents. As a consequence, the introduction of oxygen-containing adsorption sites is an important factor to achieve $Pb^{2+}$ selective adsorption, and that is the principle for the design and synthesis of most $Pb^{2+}$ adsorbents. For most of the adsorbents shown in Table S2, the exploration on selective adsorption in-depth was not mentioned.

The obtained ultrahigh adsorption selectivity for $Pb^{2+}$ in our work can be ascribed to the lower hydration energy and larger ionic radius for $Pb^{2+}$, as well as the predesigned uncoordinated oxygen-containing adsorption sites (carboxyl and ether groups) in the cage-like cavities, in which the cooperative interaction of the carboxylate and ether groups resulted in a stronger affinity for $Pb^{2+}$, leading to more selective adsorption of $Pb^{2+}$. Moreover, the close contact and sufficient interactions between the accessible sites on the exposed surface area with pollutant molecules further enhanced the adsorption selectivity, affording ultrahigh adsorption selectivity for the **Cu-MOF** nanosheets.

**Table S3.** Selective adsorption parameters of bulk **Cu-MOF** toward $Pb^{2+}$.

| Metal ions | $C_0$ (ppm) | $Pb^{2+}$ removal rate (%) | $K_d$ (mL $g^{-1}$) |
|---|---|---|---|
| $Pb^{2+}/M^{n+}$ | 10/0 | 91.62 | $1.09 \times 10^5$ |
| $Pb^{2+}/M^{n+}$ | 10/10 | 79.36 | $3.85 \times 10^4$ |
| $Pb^{2+}/M^{n+}$ | 10/50 | 60.18 | $1.51 \times 10^4$ |

**Section 5. Supporting Scheme**

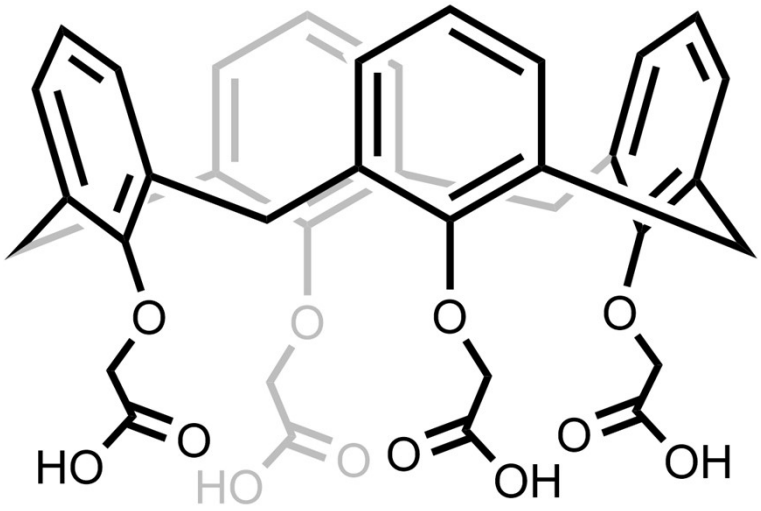


**Scheme S1.** Molecular structure of $H_4L$.

**Section 6. Supporting Figures**

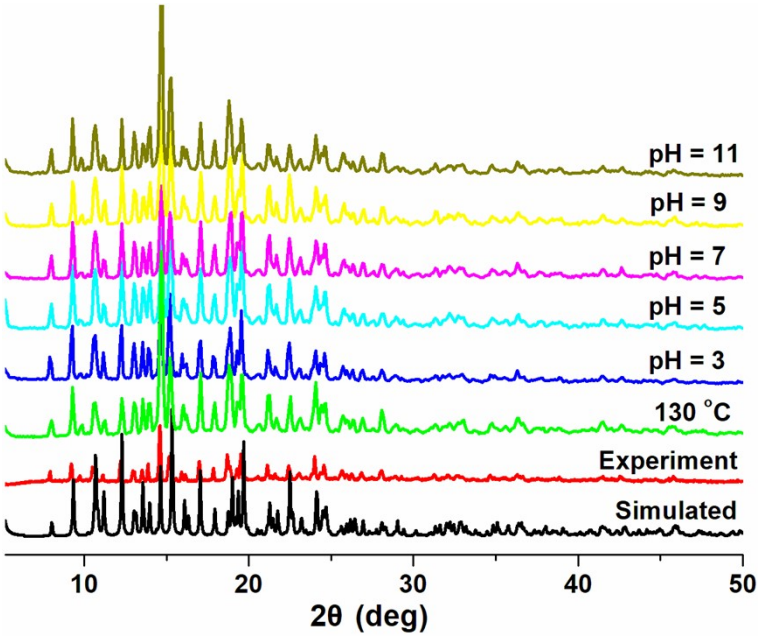


**Figure S1.** PXRD patterns of the simulated **Cu-MOF**, as-synthesized **Cu-MOF**, activated **Cu-MOF** (130 °C) and **Cu-MOF** after being immersed in an aqueous solution at pH = 3, 5, 7, 9, 11 (24 hours).

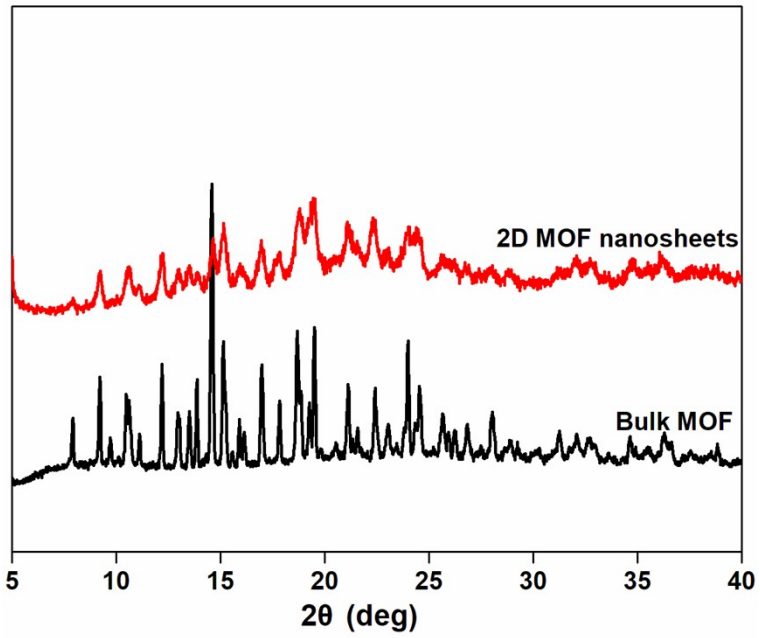


**Figure S2.** PXRD patterns of bulk **Cu-MOF** and 2D **Cu-MOF** nanosheets.

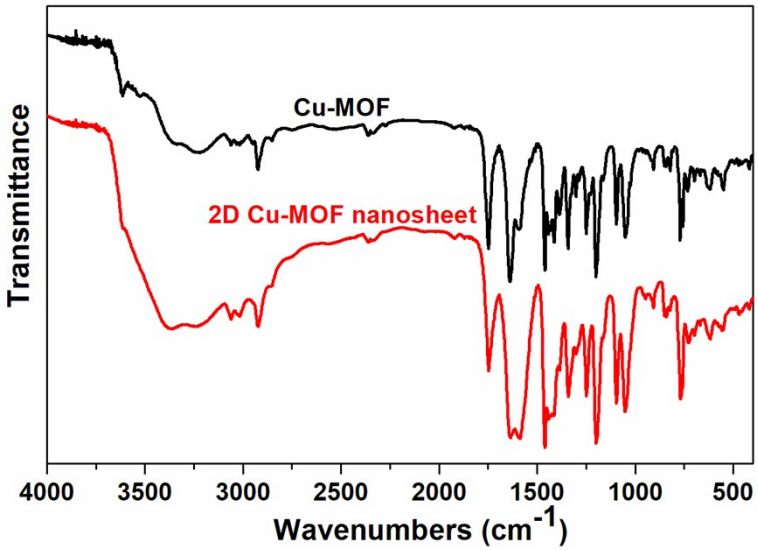


**Figure S3.** FT-IR spectra of bulk **Cu-MOF** and 2D **Cu-MOF** nanosheets.

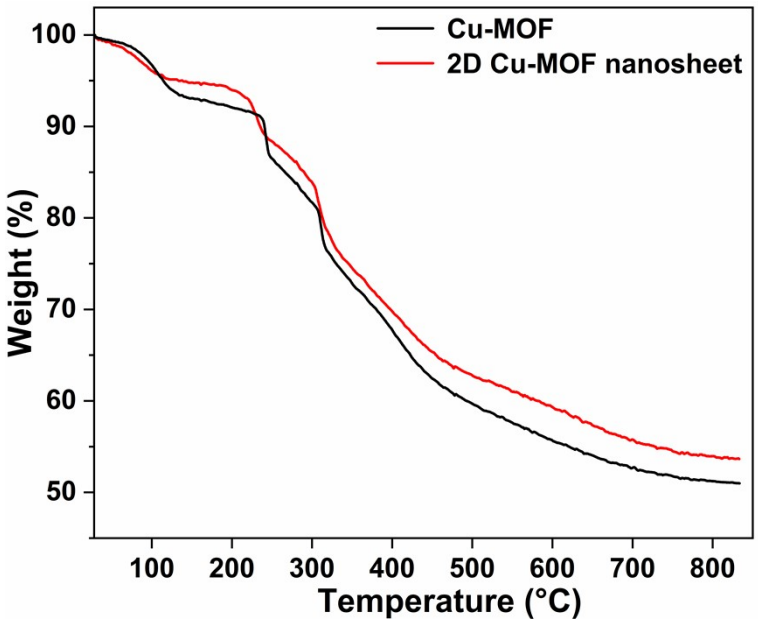


**Figure S4.** TGA curves of bulk **Cu-MOF** and 2D **Cu-MOF** nanosheets.

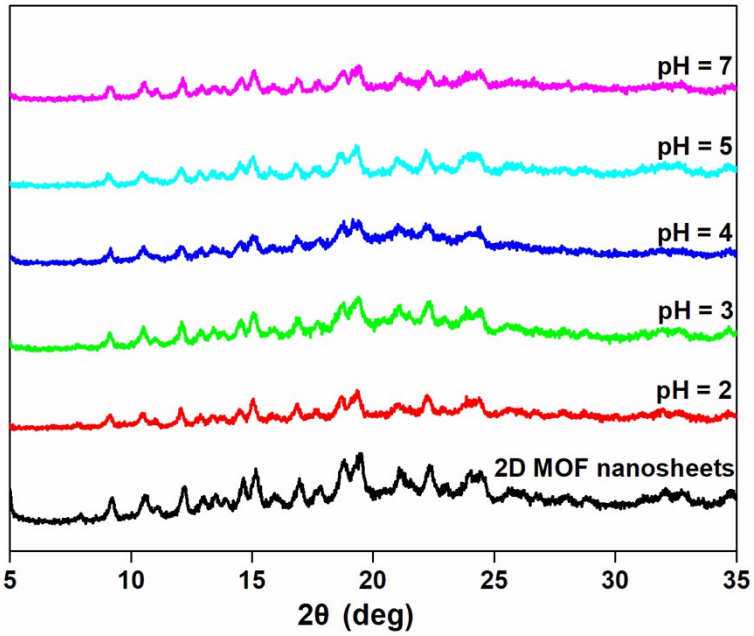


**Figure S5.** PXRD patterns of 2D **Cu-MOF** nanosheets after immeresing in aqueous solution at pH = 2, 3, 4, 5, 7 (12 hours).

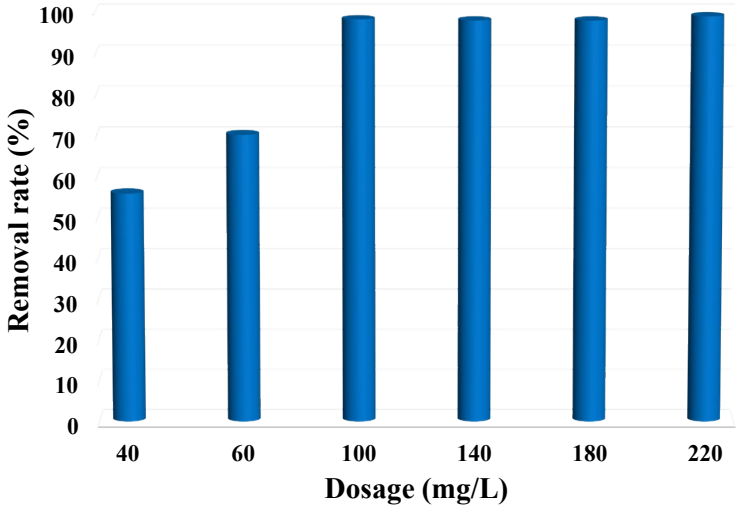


**Figure S6.** Effect of adsorbent dosages on $Pb^{2+}$ (10 ppm) adsorption by MOF nanosheets.

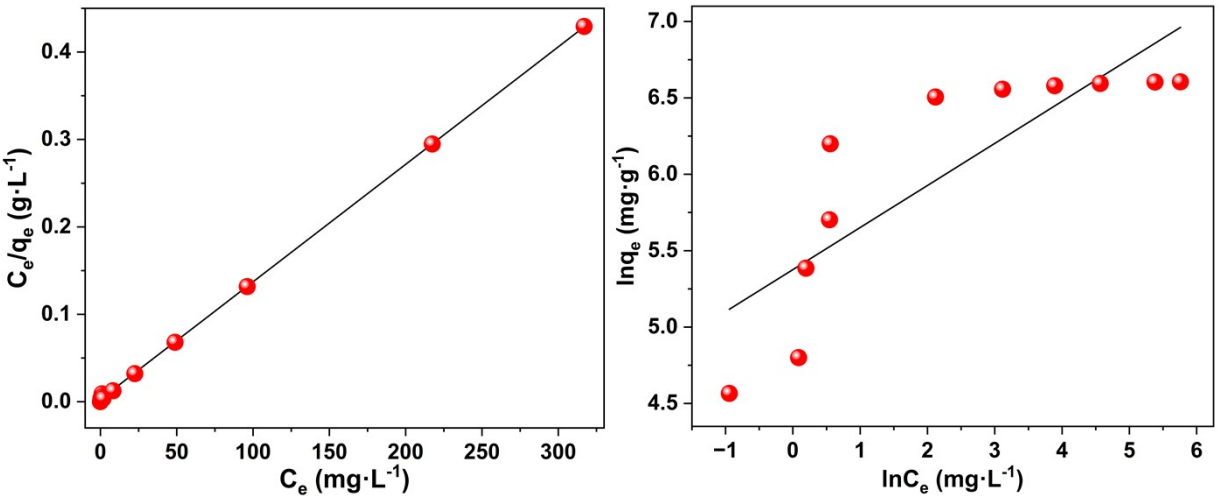


**Figure S7.** Langmuir model (a) and Freundlich model (b) fitting for $Pb^{2+}$ sorption by MOF nanosheets.

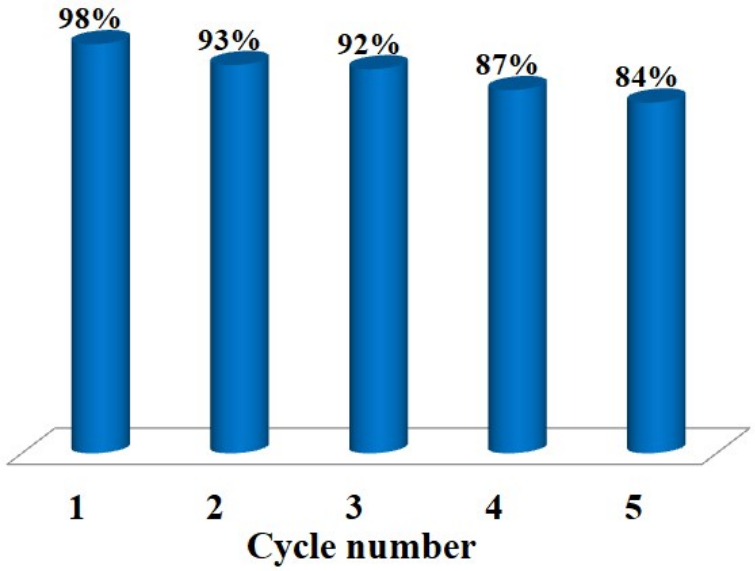


**Figure S8.** Reusability of MOF nanosheets for $Pb^{2+}$ adsorption.

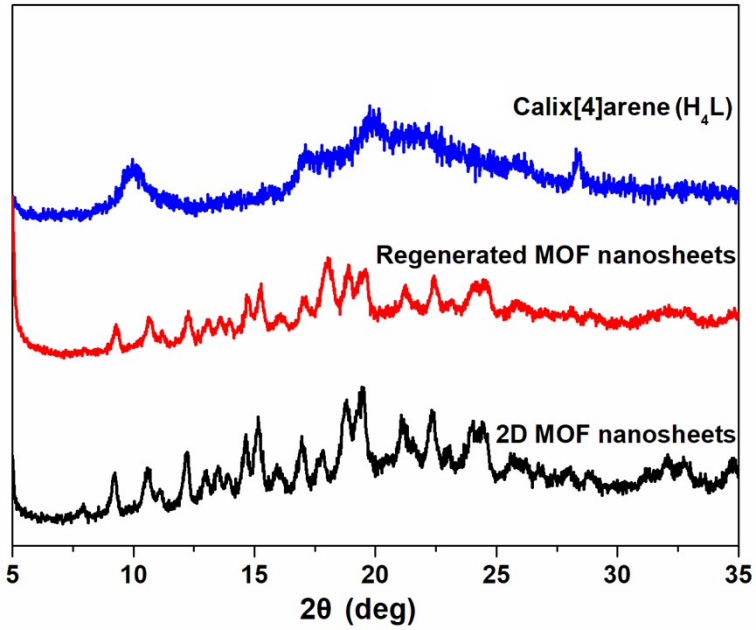


**Figure S9.** PXRD patterns of MOF nanosheets, the regenerated MOF nanosheets, and calix[4]arene ($H_4L$).

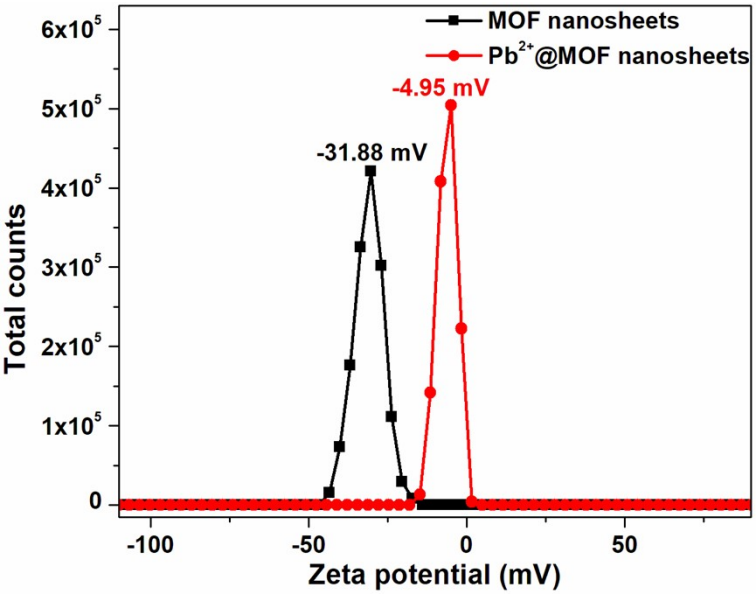


**Figure S10.** Zeta potentials of MOF nanosheets and $Pb^{2+}$@MOF nanosheets.

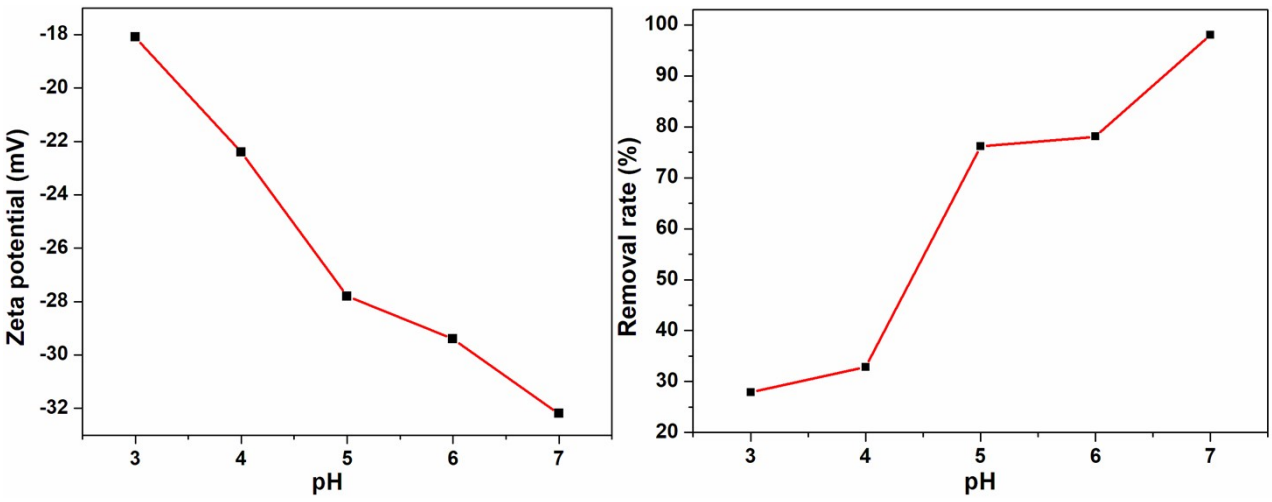


(**a**) (**b**)

**Figure S11.** (a) Effect of pH on zeta potentials of MOF nanosheets. (b) Effect of pH on $Pb^{2+}$ sorption by MOF nanosheets.

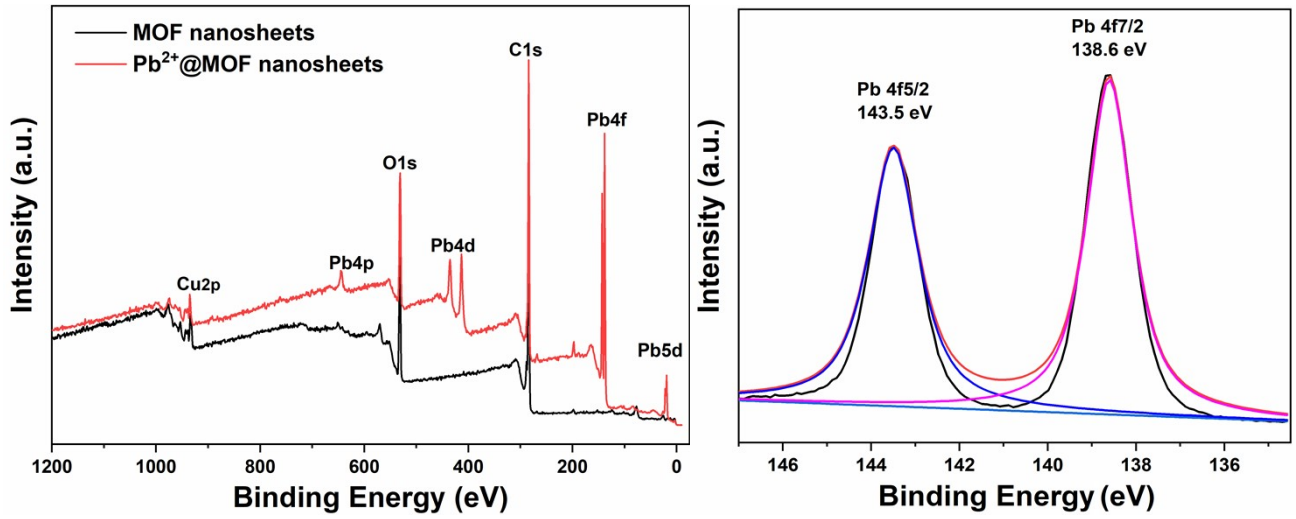


(**a**) (**b**)

**Figure S12.** (a) XPS survey of MOF nanosheets and $Pb^{2+}$@MOF nanosheets. (b) Pb 4f XPS of $Pb^{2+}$@MOF nanosheets.

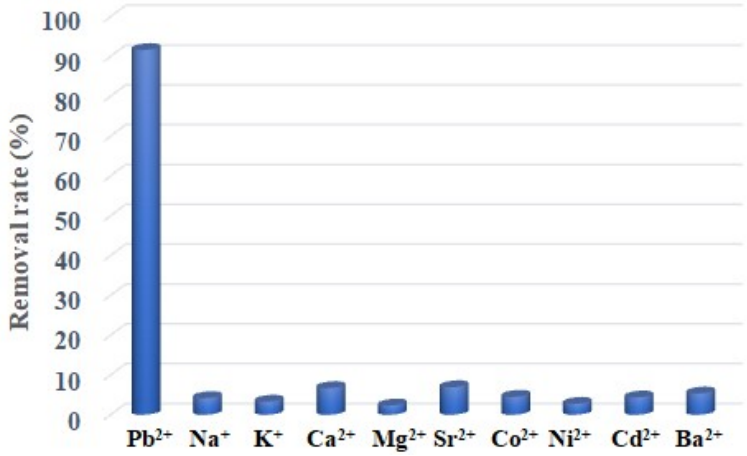


**Figure S13.** Selective adsorption of bulk **Cu-MOF** for different metal ions.

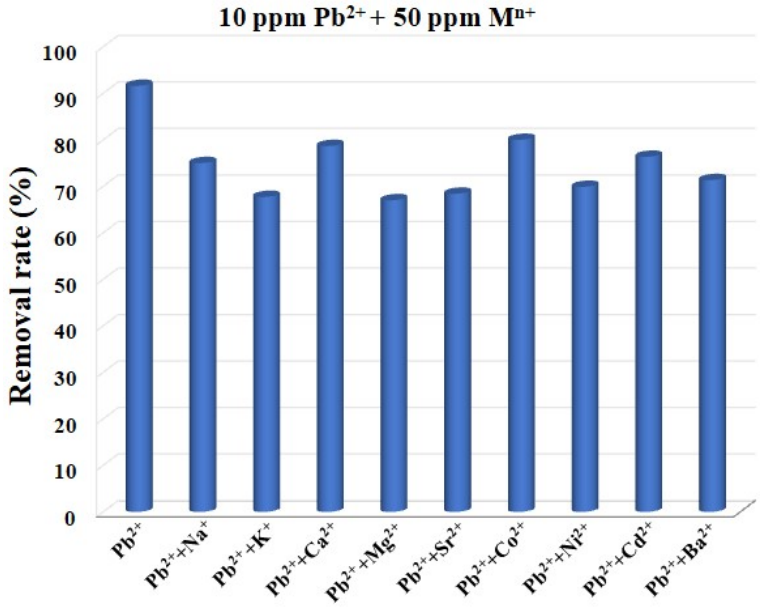


**Figure S14.** Effect of the coexistent ions (50 ppm) on $Pb^{2+}$ (10 ppm) removal by bulk **Cu-MOF**.

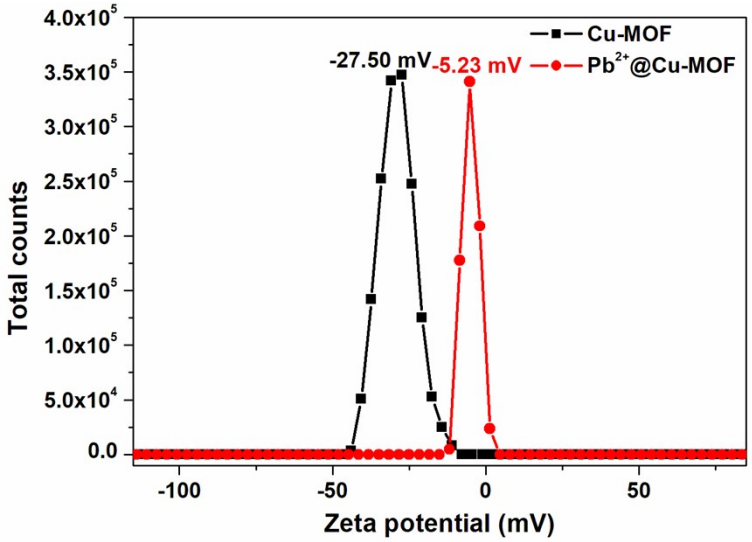


**Figure S15.** Zeta potentials of bulk **Cu-MOF** and $Pb^{2+}$@**Cu-MOF**.

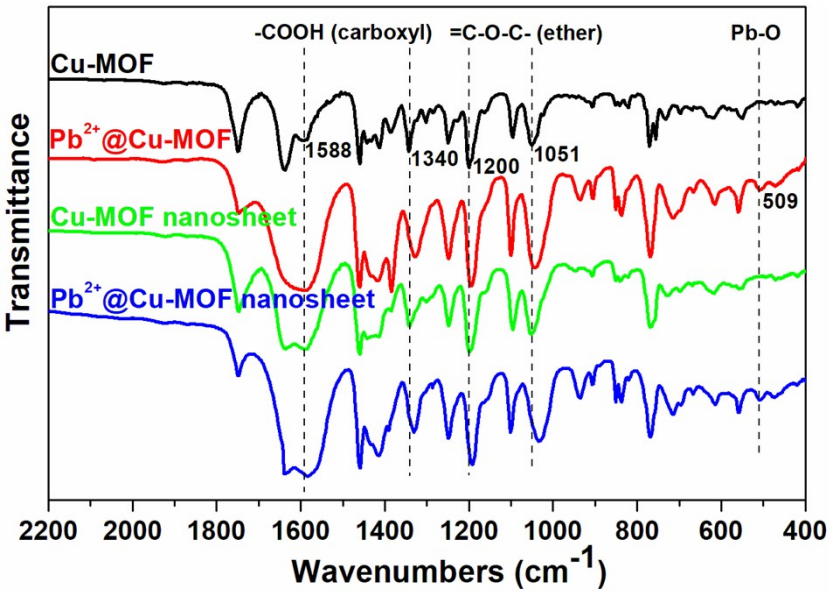


**Figure S16.** Comparison of the FT-IR spectra at 400-2200 $cm^{-1}$ for bulk **Cu-MOF**, $Pb^{2+}$@Cu-MOF, 2D MOF nanosheets, and $Pb^{2+}$@MOF nanosheets.

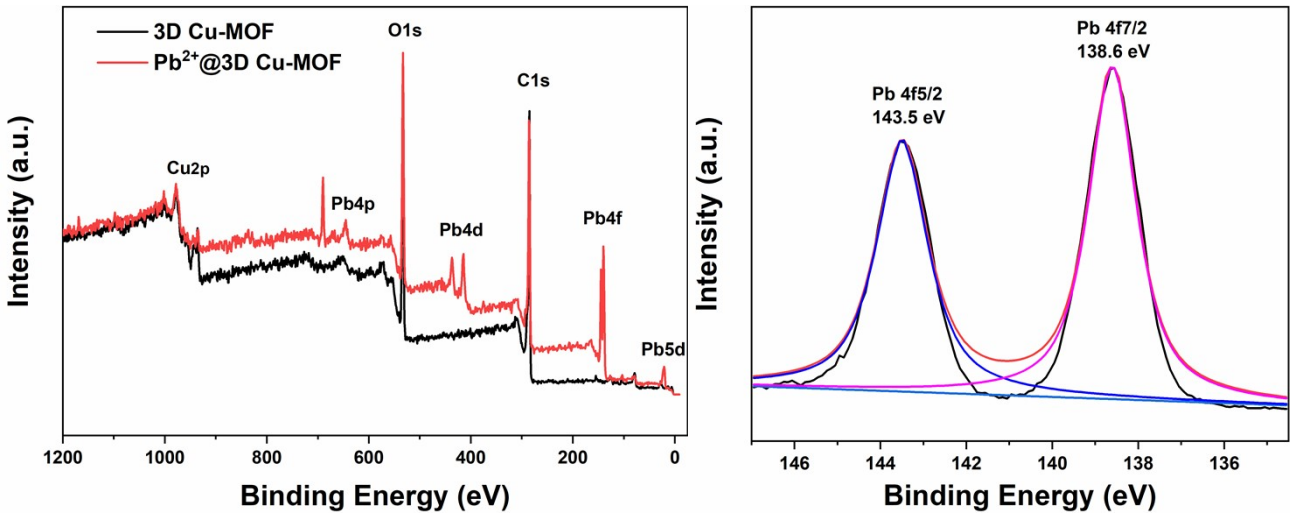


**Figure S17.** (a) XPS survey of **3D Cu-MOF** and $Pb^{2+}$@**3D Cu-MOF**. (b) Pb 4f XPS of $Pb^{2+}$@**3D Cu-MOF**.

**Adsorption mechanism of 3D Cu-MOF.** To understand the adsorption behavior of 3D **Cu-MOF**, the possible mechanistic interactions between 3D **Cu-MOF** and $Pb^{2+}$ was investigated. After $Pb^{2+}$ adsorption, the zeta potential of nanosheets changed from -27.50 mV to -5.23 mV (Figure S15), which is direct evidence for electrostatic adsorption. FT-IR spectra and XPS measurements were further conducted. In Figure S16, a new peak appeared at 509 $cm^{-1}$ after $Pb^{2+}$ adsorption, corresponds to the stretching vibration of Pb–O bond, which vanished after $Pb^{2+}$ desorption, providing direct evidence of the coordination interactions between $Pb^{2+}$ and O atoms. The peak shifts of the asymmetric and symmetric vibration of the aromatic ethers (=C−O−C−), from 1200 and 1051 $cm^{-1}$ to 1194 and 1034 $cm^{-1}$ after $Pb^{2+}$ adsorption, proved the interactions between $Pb^{2+}$ and ether groups. Moreover, the peaks at 1588, and 1340 $cm^{-1}$ are attributed to the carboxyl (−COOH) vibration in MOF nanosheets, which shifted to 1589, and 1329 $cm^{-1}$ after $Pb^{2+}$ adsorption, demonstrating the coordination between carboxyl groups with $Pb^{2+}$. The interactions between MOF nanosheets and $Pb^{2+}$ were further investigated by XPS studies. The new peaks of Pb 4f, Pb 4d, and Pb 4p that emerged following $Pb^{2+}$ adsorption provided more evidence for $Pb^{2+}$ adsorption by MOF nanosheets (Figure S17a). The high-resolution XPS of Pb 4f gave detailed information on Pb species. As shown in Figure S17b, two peaks centered at 143.5 eV and 138.6 eV were attributed to Pb $4f_{5/2}$ and Pb $4f_{7/2}$, which showed a remarkable shift of 1.0 eV to lower binding energy, by comparison with $Pb^{2+}$ binding energies of purified $Pb(NO_3)_2$ that located at 144.5 eV (Pb $4f_{5/2}$) and 139.6 eV (Pb $4f_{7/2}$). The notable peak shift demonstrated a strong affinity between $Pb^{2+}$ and MOF nanosheets. The energy separation of 4.9 eV between the peaks of Pb $4f_{5/2}$ (143.5 eV) and Pb $4f_{7/2}$ (138.6 eV) further supports the notion that coordination interaction, rather than just electrostatic contact, can be accounted for $Pb^{2+}$ adsorption. These findings are coincident with zeta potential studies and FT-IR analysis,

and the strong electrostatic attractions and coordination interactions between $Pb^{2+}$ and the carboxyl/ether groups were the key factors affecting $Pb^{2+}$ adsorption.

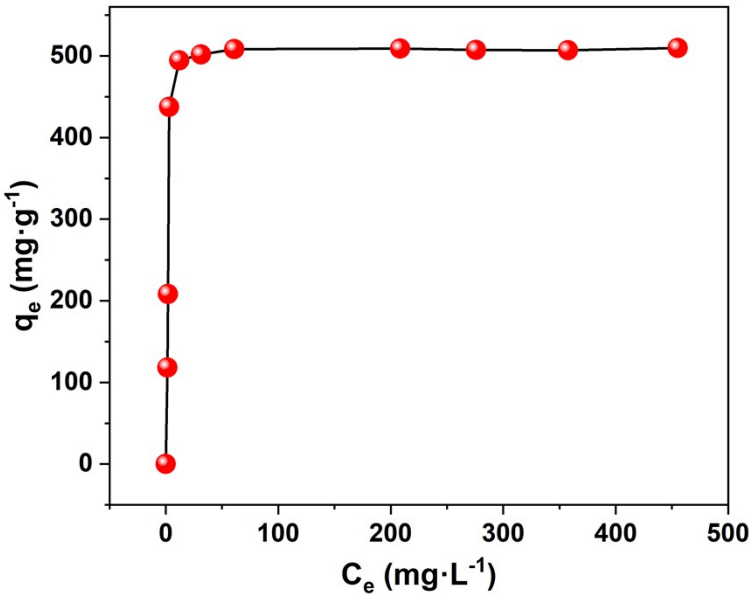


**Figure S18.** $Pb^{2+}$ adsorption isotherm for bulk **Cu-MOF**.

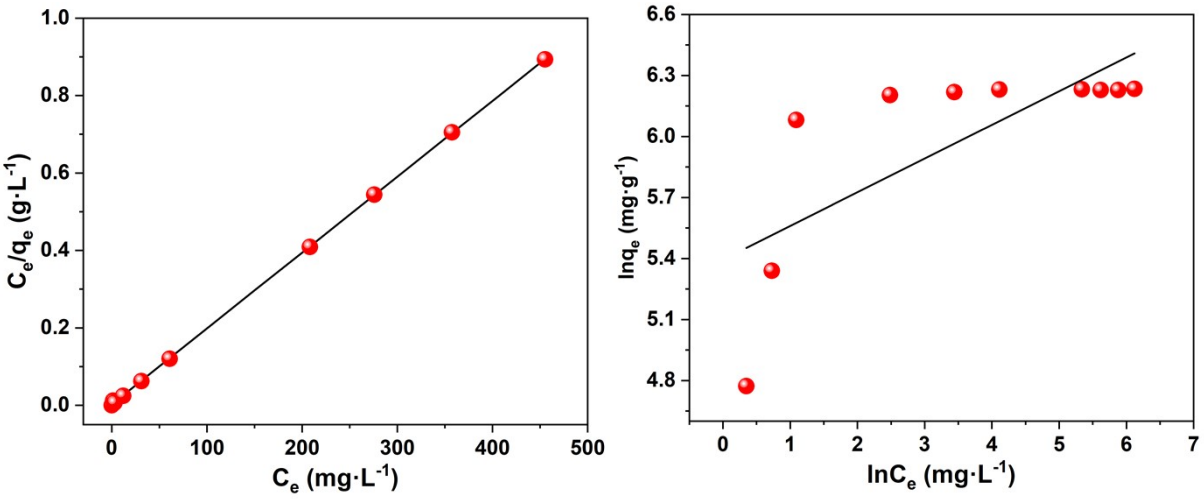


(**a**) (**b**)

**Figure S19.** Langmuir model (a) and Freundlich model (b) fitting for $Pb^{2+}$ sorption by bulk **Cu-MOF**.

**Section 7. Supporting References**

(1) Cooper, J. B.; Drew, M. G. B.; Beer, P. D. Alkali metal cation cooperative anion recognition by heteroditopic bis(calix[4]arene) rhenium(I) bipyridyl and ferrocene receptor molecules. *J. Chem. Soc., Dalton Trans.* **2000**, 2721-2728.

(2) Frisch, M. J.; Trucks, G. W.; Schlegel, H. B.; Scuseria, G. E.; Robb, M. A.; Cheeseman, J. R.; Scalmani, G.; Barone, V.; Petersson, G. A.; Nakatsuji, H.; Caricato, X. Li. M.; Marenich, A. V.; Bloino, J.; Janesko, B. G.; Gomperts, R.; Mennucci, B.; Hratchian, H. P.; Ortiz, J. V.; Izmaylov, A. F.; Sonnenberg, J. L.; Williams-Young, D.; Ding, F.; Lipparini, F.; Egidi, F.; Goings, J.; Peng, B.; Petrone, A.; Henderson, T.; Ranasinghe, D.; Zakrzewski, V.G.; Gao, J.; Rega, N.; Zheng, G.; Liang, W.; Hada, M.; Ehara, M.; Toyota, K.; Fukuda, R.; Hasegawa, J.; Ishida, M.; Nakajima, T.; Honda, Y.; Kitao, O.; Nakai, H.; Vreven, T.; Throssell, K.;Montgomery, J. A.; Peralta, J. E.; Ogliaro, F.; Bearpark, M. J.; Heyd, J. J.; Brothers, E. N.; Kudin, K. N.; Staroverov, V. N.; Keith, T. A.; Kobayashi, R.; Normand, J.; Raghavachari, K.; Rendel, A. P.; Burant, J. C.; Iyengar, S. S.; Tomasi, J.; Cossi, M.; Millam, J. M.; Klene, M.; Adamo, C.; Cammi, R.; Ochterski, J. W.; Martin, R. L.; Morokuma, K.; Farkas, O.; Foresman, J. B.; Fox, D. J.; Gaussian, Inc., Wallingford CT, **2016**.

(3) Kresse, G.; Furthmüller, J. Efficient iterative schemes for *ab initio* total-energy calculations using a plane-wave basis set. *Phys. Rev. B* **1996**, *54*, 11169-11186.

(4) Perdew, J. P.; Burke, K.; Ernzerhof, M. Generalized gradient approximation made simple. *Phys. Rev. Lett.* **1996**, *77*, 3865-3868.

(5) Kresse, G.; Furthmüller, J. Efficiency of ab-initio total energy calculations for metals and semiconductors using a plane-wave basis set. *Comp. Mater. Sci.* **1996**, *6*, 15-50.

(6) Hakimifar, A.; Morsali, A. Urea-based metal-organic frameworks as high and fast adsorbent for $Hg^{2+}$ and $Pb^{2+}$ removal from water. *Inorg. Chem.* **2019**, *58*, 180-187.

(7) Wang, R.-D.; He, L.; Zhu, R.-R.; Jia, M.; Zhou, S.; Tang, J.; Zhang, W.-Q.; Du, L.; Zhao, Q.-H. Highly efficient and selective capture Pb(II) through a novel metal-organic framework containing bifunctional groups. *J. Hazard. Mater.* **2022**, *427*, 127852.

(8) Wang, Y.; Li, M.; Hu, J.; Feng, W.; Li, J.; You, Z. Highly efficient and selective removal of $Pb^{2+}$ by ultrafast synthesis of HKUST-1: Kinetic, isotherms and mechanism analysis. *Colloids and Surfaces A* **2022**, *633*, 127852.

(9) Zhong, J.; Zhou, J.; Xiao, M.; Liu, J.; Shen, J.; Liu, J.; Ren, S. Design and syntheses of functionalized copper-based MOFs and its adsorption behavior for Pb(II). *Chin. Chem. Lett.* **2022**, *33*, 973-978.

(10) Sun, J.; Zhao, X.; Sun, G.; Zhao, H.; Yan, L.; Jiang, X.; Cui, Y. Phosphate-crosslinked β-cyclodextrin polymer

for highly efficient removal of Pb(II) from acidic wastewater. *New J. Chem.* **2022**, *46*, 3631-3639.

(11) Goyal, P.; Paruthi, A.; Menon, D.; Behara, R.; Jaiswal, A.; V, K.; Kumar, A.; Krishnan, V.; Misra, S. K. Fe doped bimetallic HKUST-1 MOF with enhanced water stability for trapping Pb(II) with high adsorption capacity. *Chem. Eng. J.* **2022**, *430*, 133088.

(12) Jiang, W.; Yu, C.-X.; Yu, M.-X.; Ding, J.; Song, J.-G.; Sun, X.-Q.; Liu, L.-L. Efficient and selective removal of $Pb^{2+}$ from aqueous solution by using an $O^{-}$ functionalized metal-organic framework. *Dalton Trans.* **2022**, *51*, 10077-10084.

(13) Zhu, R.; Zhang, P.; Zhang, X.; Yang, M.; Zhao, R.; Liu, W.; Li, Z. Fabrication of synergistic sites on an oxygen-rich covalent organic framework for efficient removal of Cd(II) and Pb(II) from water. *J. Hazard. Mater.* **2022**, *424*, 127301.

(14) Pournara, A. D.; Bika, C.-G.; Chen, X.; Lazarides, T.; Kaziannis, S.; Feng, P.; Manos, M. J. A bifunctional robust metal sulfide with highly selective capture of $Pb^{2+}$ ions and luminescence sensing ability for heavy metals in aqueous media. *Inorg. Chem. Front.* **2021**, *8*, 4052-4061.

(15) Naushad, M.; Ahamad, T.; Al-Sheetan, K. M. Development of a polymeric nanocomposite as a high performance adsorbent for Pb(II) removal from water medium: Equilibrium, kinetic and antimicrobial activity. *J. Hazard. Mater.* **2021**, *407*, 124816.

(16) Yu, C.-X.; Wang, K.-Z.; Li, X.-J.; Liu, D.; Ma, L.-F.; Liu, L.-L. Highly efficient and facile Removal of $Pb^{2+}$ from water by using a negatively charged azoxy-functionalized metal-organic framework. *Cryst. Growth Des.* **2020**, *20*, 5251-5260.

(17) Poudel, M. B.; Awasthi, G. P.; Kim, H. J. Novel insight into the adsorption of Cr(VI) and Pb(II) ions by MOF derived Co-Al layered double hydroxide @hematite nanorods on 3D porous carbon nanofiber network. *Chem. Eng. J.* **2021**, *417*, 129312.

(18) Xiong, C.; Wang, S.; Hu, P.; Huang, L.; Xue, C.; Yang, Z.; Zhou, X.; Wang, Y.; Ji, H. Efficient selective removal of Pb(II) by using 6-aminothiouracil-modified Zr-based organic frameworks: From experiments to mechanisms. *ACS Appl. Mater. Interfaces* **2020**, *12*, 7162-7178.

(19) Zarekarizi, F.; Morsali, A.; Büyükgüngor, O. Rapid and selective water remediation through a functionalized pillar's core of a novel metal-organic framework. *Cryst. Growth Des.* **2020**, *20*, 6109-6116.

(20) Ji, Z.; Sun, H.; Zhu, Y.; Zhang, D.; Wang, L.; Dai, F.; Zhao, Y.; Chen, L. Enhanced selective removal of lead ions using a functionalized PAMAM@UiO-66-$NH_2$ nanocomposite: Experiment and mechanism. *Micropor. Mesopor. Mater.* **2021**, *328*, 111433.

(21) Abdelhameed, R. M.; Ismail, R. A.; El-Naggar, M.; Zarie, E. S.; Abdelaziz, R.; El Sayed, M. T. Post-synthetic modification of MIL-125 with bis-quinoline Mannich bases for removal of heavy metals from wastewater. *Micropor. Mesopor. Mater.* **2019**, *279*, 26-36.

(22) Zhang, T.; Li, P.; Ding, S.; Wang, X. High-performance TFNC membrane with adsorption assisted for removal of Pb(II) and other contaminants. *J. Hazard. Mater.* **2022**, *424*, 127742.

(23) Shi, S.; Xu, C.; Dong, Q.; Wang, Y.; Zhu, S.; Zhang, X.; Tak Chow, Y.; Wang, X.; Zhu, L.; Zhang, G.; Xu, D. High saturation magnetization $MnO_2$/PDA/$Fe_3O_4$ fibers for efficient Pb(II) adsorption and rapid magnetic separation. *Appl. Surf. Sci.* **2021**, *541*, 148379.

(24) Chen, Y.; Tang, J.; Wang, S.; Zhang, L.; Sun, W. Bimetallic coordination polymer for highly selective removal of Pb(II): Activation energy, isosteric heat of adsorption and adsorption mechanism. *Chem. Eng. J.* **2021**, *425*, 131474.

(25) Li, J.; Zhao, Z.; Song, Y.; You, Y.; Li, J.; Cheng, X. Synthesis of Mg(II) doped ferrihydrite-humic acid coprecipitation and its Pb(II)/Cd(II) ion sorption mechanism. *Chin. Chem. Lett.* **2021**, *32*, 3231-3236.

(26) Motaghi, H.; Arabkhani, P.; Parvinnia, M.; Javadian, H.; Asfaram, A. Synthesis of a highly porous three-dimensional PVA/GO/ZIF-67 cryogel for the simultaneous treatment of water contaminated with cadmium(II) and lead(II) heavy metal ions. *New J. Chem.* **2022**, *46*, 4449-4461.

(27) Geisse, A. R.; Ngule, C. M.; Genna, D. T. Removal of lead ions from water using thiophene-functionalized metal-organic frameworks. *Chem. Commun.* **2020**, *56*, 237-240.

(28) Qiao, X.-X.; Liu, G.-F.; Wang, J.-T.; Zhang, Y.-Q.; Lü, J. Highly efficient and selective removal of lead ions from aqueous solutions by conjugated microporous polymers with functionalized heterogeneous pores. *Cryst. Growth Des.* **2020**, *20*, 337-344.